ORIGINAL RESEARCH

Ecospheric Decontamination Attained via Green Nanobiotechnological NiO-Based Nanocatalyst Derived from Nature's Biofactories

Taghazal Zahra[1]
Khuram Shahzad Ahmad [1]
Dauod Ali[2]

[1]Department of Environmental Sciences, Fatima Jinnah Women University, Rawalpindi, Pakistan; [2]Department of Zoology, College of Sciences, King Saud University, Riyadh 11451, Saudi Arabia

Introduction: Water contamination from dye effluents from various industrial sources has become a major challenge of the scientific community that is difficult to remediate using orthodox chemical and biological procedures. As such, there is a need for more suitable and cost-effective ways to treat such effluents. The present work describes a green-synthesis approach for preparation of three types of Ni-based oxides as effective catalytic materials to remove environmental pollutants. Metal oxide nanomaterials are cheap, abundant, and ecofriendly earth metals, and thus are promising materials for catalytic applications for environmental detoxification.

Methods: An aqueous leaf extract of *Prunus persica* was used as a reducing agent for the synthesis of NiO, NiO–PdO, and NiO–ZnO nanoparticles (NPs). The leaf extract was treated with each metal-salt precursor based on sol–gel synthesis, and then the final procured NPs were analyzed by spectroscopic techniques for structural and morphological makeup. The pure NPs were further explored for catalytic degradation of hazardous aqueous dye at ambient conditions, instead of following any sophisticated experimental conditions.

Results and Discussion: Morphological features revealed the pure formation of NiO, NiO–ZnO, and NiO–PdO NPs of size <100nm, characterized by X-ray diffraction spectroscopy and scanning electron microscopy. Catalytic tests with methyl orange revealed the remediation potential of synthesized material, showing the pseudo–first order kinetics ($R^2<1$) for NiO, NiO–PdO, and NiO–ZnO. NiO–ZnO gave outstanding results both in dark ($R^2=0.88$) and light ($R^2=0.82$) with degradation percentage of 99% (dark) in comparison with the other two catalysts. Moreover, excellent catalyst stability for NiO–ZnO) was observed, even after the fourth cycle, under both light and dark conditions and was separated easily during centrifugation.

Conclusion: Although all three materials depicted the degradation potential with good stability, but the NiO–ZnO catalyst was the best catalytic material in the present investigation, with prominent degradation percentage, and can be considered as an efficient catalytic material. Thus, we conclude that *P. persica*–inspired catalytic material could pave the path toward environmental remediation, alternative clean energy, and other biological applications.

Keywords: bioinspired, nanocatalyst, methyl orange, environmental remediation, catalytic

Introduction

Organic dyes are one of the main groups of chemical compounds used widely in textiles, food, cosmetics, and the pharmaceutical industry. They are considered as the major source of contaminants, but are still in major demand in these industries.

Correspondence: Khuram Shahzad Ahmad
Email chemist.phd33@yahoo.com

These industries release a lot of dye as waste material that dissolves readily in local water bodies at a concentration of 10–200 mg/L, resulting in eutrophication and reduced potential for reoxygenation, eventually causing extreme impairment of marine flora and fauna by impeding sunshine infiltration.[1–4] Protection of water bodies from toxic contaminants is the prime focus of researchers at present, as conventional methods used for detoxification of such wastewater toxicants that are highly resistant to microorganisms are not very effective.[5,42]

Nanotechnology advancement has become an important focus of scientific exploration in physics, chemistry, and engineering. Metal nanoparticles (NPs) display distinct features directly related to the size and shape of the particles.[6–8] Metal and metal oxide NPs have been found to be suitable candidates for such applications as wastewater treatment, pharmaceuticals, medical diagnosis, and drug-delivery systems. Currently, environmental projects that use green chemistry to enhance and preserve our global environment are becoming the subject of many research fields.[7–9] This has paved the way for greener NP synthesis and proved promising, due to slower kinetics and better manipulation and regulation of crystal growth and stabilization. This has created a spark in research on synthesis approaches that enables better control of shape and size for different nanotechnological applications.[10] Instead of using harmful reagents as reducing and stabilizing agents in the synthesis of metallic NPs, significant attention has been paid to the use of different biological entities in the field of nanobiotechnology.[11,12] Biologically active plant products provide excellent scaffolds among the many possible natural products. Phytochemicals play an important role in both reduction and stabilization of NPs, and have emerged as an important natural resource for the synthesis of metal/metal oxide NPs among potential bioactive compounds categorized in plants.[12,13]

Metal oxide NPs are most suitable candidates for removal of wastewater contaminants, as oxygen atoms present on the surface constrain the charge carriers' recombination for longer periods.[14,15] The hydroxyl and carboxyl functional groups in metal oxide–based material reveal remarkable hydrophilicity and negative-charge density to degrade organic pollutants in the water environment. Previously, these functional groups were procured from synthetic carbon-based compounds, ie, carbon nanotubes and carbon black or graphene oxide.[15–17] However, in the present investigation these functional groups were introduced from a natural source: *Prunus persica* leaf extract. The present work focuses on implementation of the factual principles of green chemistry in the synthesis of nickel-based oxide NPs by using a stand-alone reduction and capping agent: *P. persica* leaf extract in aqueous medium. The synthesized particles were used further for deterioration of azo dye under dark ambient conditions. Single-metal and metal oxide NPs[18–22] have been synthesized with a biobased approach, but the uniqueness of the present work is that it is based on synthesis of binary compounds that have not been reported previously with *P. persica*. Similar studies have focused on synthesis procedures, structure, and morphology, whereas the present investigation studied phytofunctional groups in synthesized material with gas chromatography–mass spectroscopy (GC-MS) also. The synthesized particles successfully decomposed an aqueous solution of methyl orange (MO) within 20 minutes of reaction, not only under light conditions but also under dark ambient conditions without any additional stimulant. We believe the incorporated functional groups speed up the catalytic efficiency of synthesized material due to C–O–M bonding.

Methods
Chemicals

Metal salts, i.e, nickel(II) acetate tetrahydrate (Ni $[CH_3CO_2]_2 \cdot 4H_2O$), zinc acetate (ZnO$[CH_3COO]_2$), and palladium(II) acetate (Pd$[CH_3COO]_2$) were purchased from Merck Chemicals. All experimentation was done with deionized water (DI), and apparatus was sterilized with C_2H_5OH. Reducing-cum-stabilizing agents were extracted from foliar extracts of *P. persica* collected from AJK Pakistan. Sample leaves were shade-dried, extracted with DI, and stored at 4°C for utilization as a reducing agent and for phytochemical screening.

Synthesis of Organic Extract–Derived NiO, NiO–PdO, and NiO–ZnO Nanocatalysts

In typical green-functionalization mode, catalysts (NiO, NiO–ZnO, and NiO–PdO NPs) were prepared by reacting metal salts with foliar extract of *P. persica* without any utilization of chemical reducing agents. Each metal salt solution (20 mM) was prepared by taking Ni $(CH_3CO_2)_2.4H_2O$, ZnO$(CH_3COO)_2$ and Pd $(CH_3COO)_2$ in seperate beakers containing 100 mL of DI water and stirred for 15 mins for complete dissolution. With no residues left, the homogeneous reaction mixtures

were mixed in a 500 mL beaker and 10 mL *Prunus persica* foliar extract was added slowly with continuous stirring. The reaction mixture comprising the organic–inorganic complex, ie, metal salt–*P. persica* foliar extract] was heated at 80°C with continuous stirring. Stabilization and subsequent conversion of a metal salt–*Prunus* persica foliar extract to NiO, NiO–ZnO, and NiO–PdO NPs were confirmed via immediate visual transformation indicating NPs formation. For further homogenization, the reaction mixture containing metal oxide NPs was incubated overnight, followed by centrifugation at 6,000 rpm for 20 minutes for pellet formation. Upon centrifugation, dark-brownish precipitates settled at the bottom of the centrifugation tubes, which were washed with DI water and ethanol. Collected precipitates were dried at 95°C using an oven, followed by calcination in a furnace at 450°C for elimination of any residual organic compounds from the foliar extract after stabilization. The finally calcined NiO, NiO–ZnO, and NiO–PdO NPs were stored in labeled eppendorf tubes for further catalytic experimentation.

Characterization

In the current work, the *P. persica* foliar extract was characterized for functional groups and biomolecules responsible for metal oxide synthesis using Fourier-transform infrared (FTIR)_spectroscopy (8400; Shimadzu, Kyoto, Japan) and GC-MS (QP5050; Shimadzu) using KBr pelletization and organic extraction, respectively. In addition to the foliar extract, NiO, NiO–ZnO, and NiO–PdO NPs were characterized by such analytical techniques as FTIR spectroscopy for vibrational and molecular arrangements spanning 4,000–400 cm^{-1}. Lattice parameters and crystallinity were studied using powder X-ray diffractometer (XRD; Bruker D9). Morphological investigation was done via field-emission scanning electron microscopy (FE-SEM; Quanta 250-FEG)-coupled energy-dispersive X-ray spectroscopy for elemental signaling. Optical response of NPs was done via ultraviolet-visible (UV-vis) spectroscopy (1602; Biomedical Services, Spain), and Tauc plots were used for band-gap calculation.

Catalytic Experiments

The photocatalytic behavior of biogenically synthesized NPs was demonstrated by removing the hazardous dye MO and observing the effect in light and dark conditions. A stock solution of MO (1 L) was prepared in double-distilled water at a ratio of 1:1 (1 mg/mL). For catalytic activity, 2 mg synthesized NiO, NiO–ZnO, and NiO–PdO

NPs were added separately into 20 mL test tubes containing 10 mL MO and mixed ultrasonically for 15 minutes. For observation of adsorption in the dark, the test tubes were covered with aluminum foil. Afterward, 3 mL of each solution was taken to evaluate catalytic reactions at different time intervals on UV-vis spectroscopy at 200–800 nm. Absorbance was compared with the lambda maxima of MO. A controlled set was also prepared in similar experimental conditions without a catalyst and results were compared. By measuring the lambda maxima for all samples at different time intervals, a linear calibration curve was obtained for all samples presenting the regression value. After that, percentage degradation was calculated by observing the decrease in absorption intensity at 460 nm:[23,24]

$$Degradation(\%) = Ct/C0*100 \qquad (1)$$

where C_t and C_0 represent final and initial concentration, respectively.

Results and Discussion

The plant extract was subjected to UV, FTIR and GC-MS spectroscopy to identify the bioactive compounds that play a role in the synthesis process. Analysis revealed the presence of alcoholic and phenolic compounds depicted in Figure 1 (S-1). FTIR analysis of synthesized material was done to demonstrate the functional group scanned at 4,000–400 cm^{-1}. In Figure 1A, the FTIR spectrum of NiO show absorption peaks at 1,113.68 cm^{-1} and some vibrations at 1,300 cm^{-1} and 1,500 cm^{-1}, corresponding to nitro compound N–O symmetrical stretch and aromatic C–C stretch.

The inset depicts the range 600–400 cm^{-1}, showing sharp vibrations at 480 cm^{-1}, 477 cm^{-1}, and 426 cm^{-1} corresponding to the M–O bond (metal oxygen). Similarly NiO–PdO showed vibrations at 1,957 cm^{-1}, 1,355 cm^{-1}, and 625 cm^{-1}, presenting water adsorption on the surface of pellets, C–H rock, and C–Cl stretch (metal halides), which may have been due to KBr. Below 500 cm^{-1}, strong absorption at 499 cm^{-1} and 426 cm^{-1} demonstrated the metal–oxygen bond. All the other peaks removed during calcinations as organic compounds were mostly removed at high thermal treatment.[26] NiO-incorporated ZnO spectra presented in Figure 1C show vibrations at frequency of 2,038.69 cm^{-1}, 1,374.19 cm^{-1}, and 1,104.24 cm^{-1} corresponded to N–O symmetrical stretch due to nitro compounds and aliphatic amines or C–O stretch due to alcohols and carboxylic acids. Mostly, vibration at 1,800–2,100 cm^{-1}
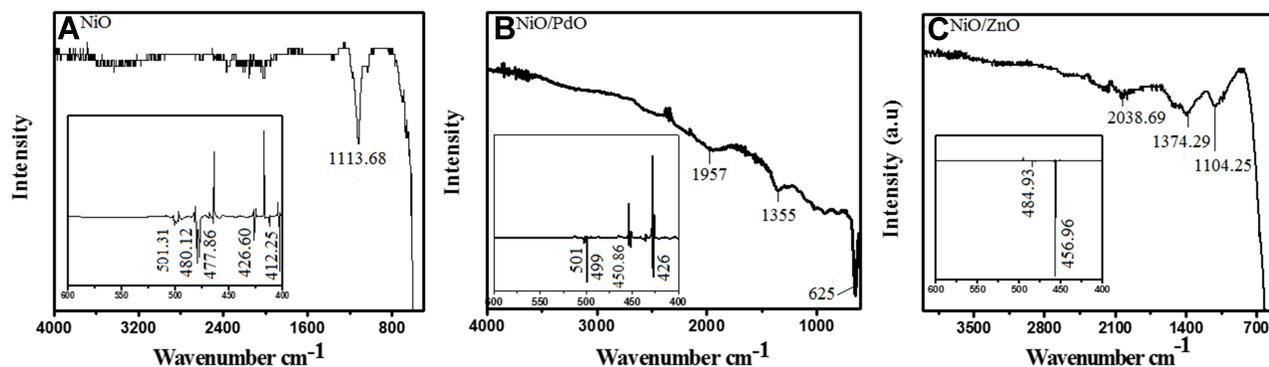
Figure 1 FTIR spectra of biosynthesized nanomaterials: (**A**) NiO; (**B**) NiO–PdO; (**C**) NiO–ZnO.

depicted the hydroxyl group, due to water adsorption on the surface. A sharp peak at 456.96 cm^{-1} in the inset (1-c) shows the M–O bond. In all three materials, strong fingerprint vibration <500 cm^{-1} pointed to M–O, M–OH, and M–C bonds (metal oxide).[26–28] Therefore, FTIR-spectroscopy analysis anticipated the involvement of phyto-functional groups along with fingerprinting of metal oxides.

GC-MS analysis further endorsed the presence of functional compounds as capping agents in the synthesized nanomaterial, as depicted in Figure 2. GC-MS of NiO (Figure 2A) showed the presence of octodrine, benzene–ethane amine, and decanoic acid at retention times of 4.932, 5.489, and 28.842 minutes, respectively. NiO–PdO showed peaks at 20.46 and 21.56 minutes, corresponding to octadecanoic acid–octodrine or cyclobutanol. Figure 2C show GC-MS of NiO–ZnO with sharp vibration at 20.909 minutes' retention, depicting the presence of octodrine or cyclobutanol. The same phytocompounds were probed in *P. persica* plants (SI), which confirmed functional group incorporation in synthesized metal oxides congruent to FTIR-spectroscopy analysis.

Chemical and composition analysis of all three *P. persica*–mediated nanomaterials was further carried out with Raman spectroscopy, which validated metal oxide formation and organic compound involvement. NiO (Figure 3A) showed characteristic Raman bands at 497 cm^{-1}. Peaks around 500 cm^{-1} corresponded to NiO in comparison with previous literature.[29] NiO-PdO exhibited a sharp peak at 649.35 cm^{-1} and some vibrations between 800 and 1,500 cm^{-1} were observed, as in Figure 3B, which might be associated with the organic compounds. Similarly, the spectrum of NiO–ZnO in Figure 3C depicts vibration at 506 cm^{-1} and >1,100–3,500 cm^{-1}. The peak at 506 cm^{-1} clearly demonstrated characteristics of Ni-incorporated ZnO, as metal oxides show vibration at frequencies of 400–800 cm^{-1}. In all three spectra, vibration peaks >800 cm^{-1} validated the presence of bioactive functional groups, in good agreement with FTIR-spectroscopy analysis.

The crystal structure, phase, and composition of biosynthesized NiO and hybrid NiO-ZnO, NiO-PdO were analyzed by XRD (Figure 4A–C). Sharp narrow peaks with 2θ
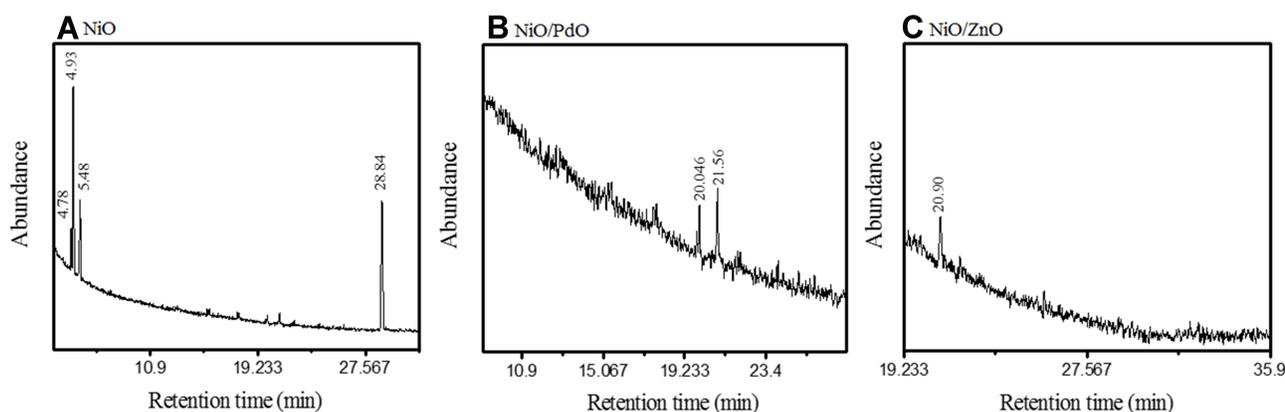
Figure 2 GCMS chromatograms of (**A**) NiO, (**B**) NiO–PdO, and (**C**) NiO–ZnO.
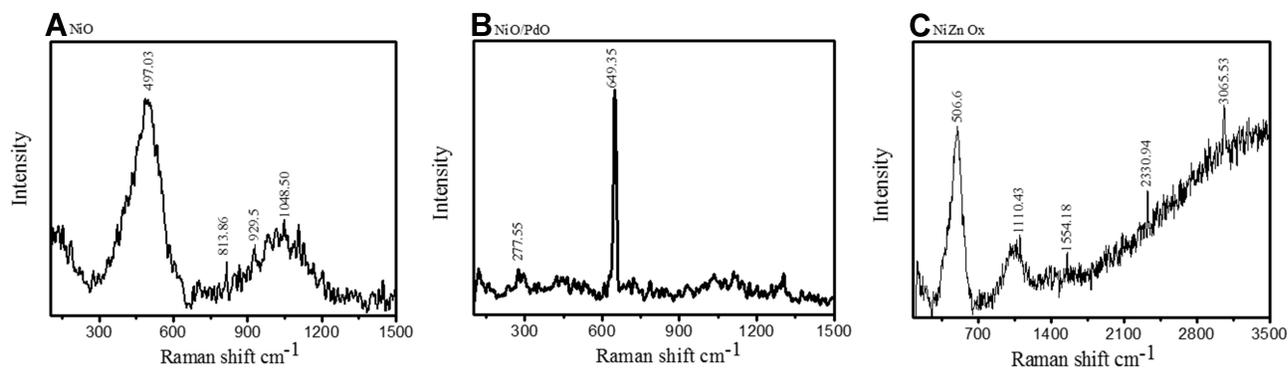
Figure 3 Characteristic Raman spectra of (**A**) NiO, (**B**) NiO–PdO, and (**C**) NiO–ZnO.
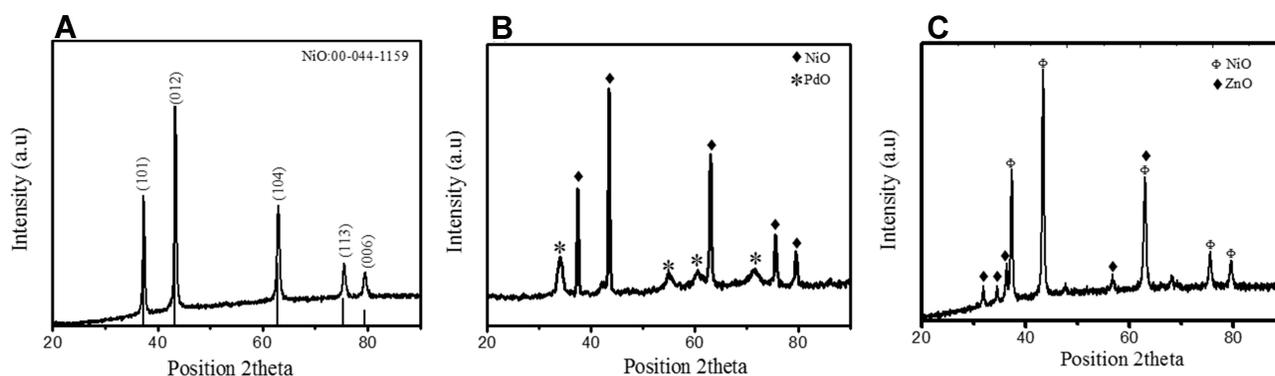
Figure 4 XRD diffractograms of synthesized (**A**) NiO, (**B**) NiO–PdO, and (**C**) NiO–ZnO.

values of 37.1, 43.3, 63.2, 75.86, and 79.2 were indexed as (101), (200), (012), (110), and (113) crystal planes. These planes confirmed the pure formation of crystalline rhombohedral symmetry of NiO NPs (Figure 4A), in good agreement with Joint Committee on Powder Diffraction Standards card 00–044-1159. NiO-incorporated PdO showed two phases, ie, NiO and PdO, in good agreement with 00–022-1189 and 00–041-1107, respectively. In Figure 4B, diffraction peaks indicated by (♦) at 2θ values of 37.24°, 43.25°, and 75.40° were associated with (003), (012), and (104), respectively, in close match with literature values for NiO. PdO exhibited a tetragonal crystal system with cell parameters of $a = 3.04$, $b = 3.04$, and $c = 5.3$Å, and introduce characteristic peaks denoted by (*) at 2θ = 33.83°, 54.71°, and 60.78° with corresponding Miller indices (101), (112), and (200) respectively. Similarly, XRD patterns of NiO–ZnO demonstrated reflection peaks of both ZnO and NiO (Figure 4C), with references 00–044-1159 and 00–005-0664, respectively. In NiO–ZnO hybrid material, NiO exhibited a rhombohedral crystal structure with Miller indices at (101), (012), (104),

(113), and (202) represented by (ɸ), while ZnO (♦) presented a hexagonal structure with *hkl* indices (100), (002), (102), and (110), corresponds to 31.75, 35.44, 47.54, and 56.55 peak positions.

Using the Scherrer equation (eq. 2), grain size was calculated as:

$$D = (0.9 \; x \; \lambda)/(\beta \; cos\theta) \qquad (2)$$

where λ refers to wavelength and β is full width at half-maximum intensity of the peak. Average grain size calculated for synthesized NiO, NiO–PdO, and NiO–ZnO was 17.42, 12.6–7.42, and 7.83–9.07, respectively. Surface morphology of prepared nanostructures calcined at 450°C was examined by FE-SEM, as shown in Figure 5A–C. The surface of NiO was found to be relatively smooth and particles were evenly distributed with no agglomeration, as in Figure 5A. When PdO particles were loaded on NiO, the surface showed some agglomeration due to incorporation of palladium oxide, but still the particles were uniformly distributed at nanoscale.
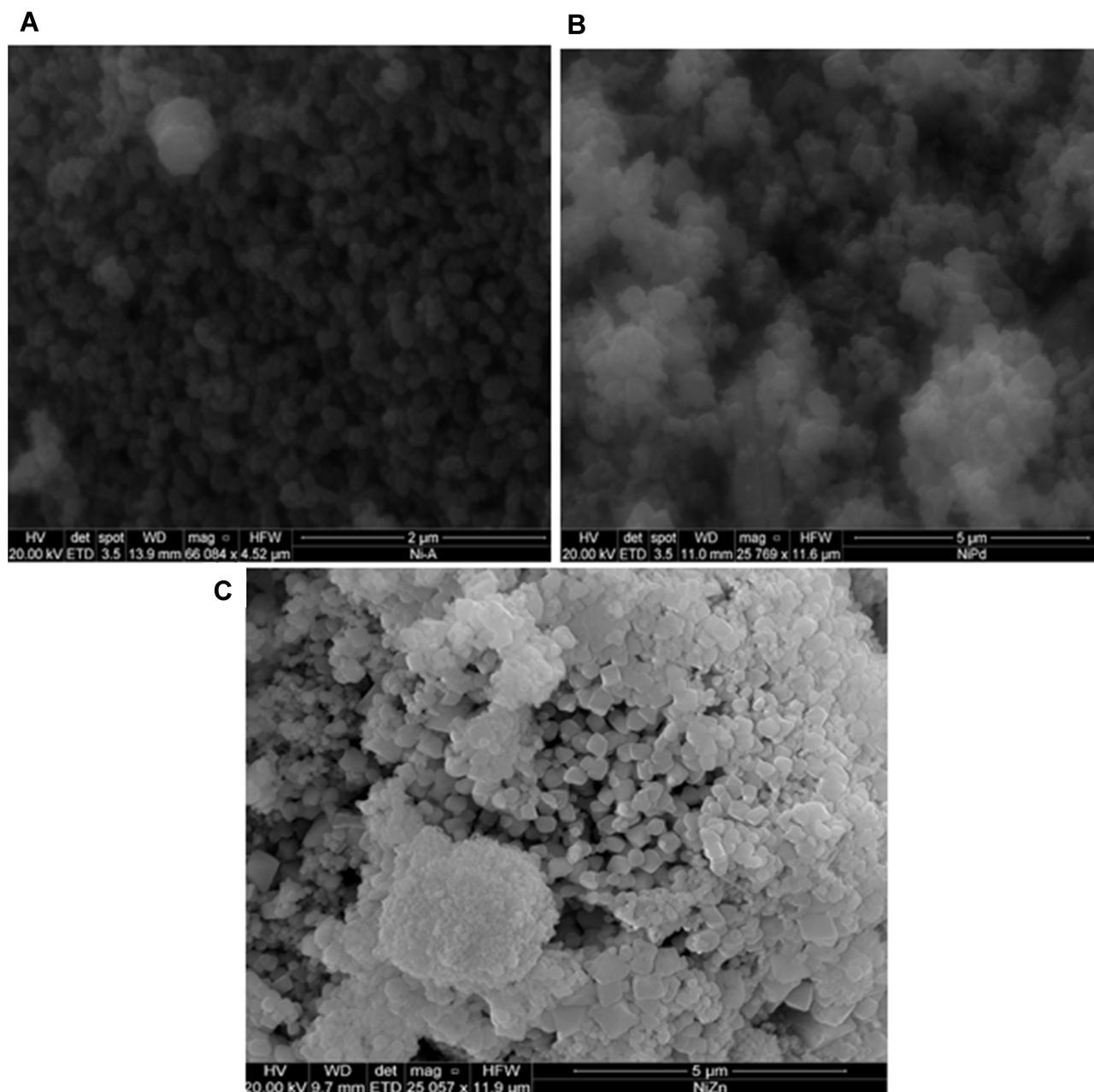
Figure 5 FE-SEM of biosynthesized nanomaterials: (**A**) NiO, (**B**) NiO–PdO, and (**C**) NiO–ZnO.

It can be seen in Figure 5B and C that cavities and channels were formed, which support the ease of post operational separation of catalyst from wastewater.[30,31] Figure 5C shows clear and defined cuboid nanostructures with voids and spaces showing minimum or no agglomeration. These internal spaces and cavities support the process of catalysis. Therefore, biogenically synthesized nanomaterials not only reduced size to nanoscale but uniformly distributed the particles as well. SEM revealed nanoscale synthesis of NiO, NiO–PdO, and NiO–ZnO

consistently with the crystallite size obtained by XRD, with lowest size for NiO–ZnO nanomaterial. Although XRD revealed the lowest crystallite size for NiO–ZnO, in SEM it was apparent that of NiO–ZnO particles were clearer and somehow larger than the other two oxides, which may be attributed to the fact that XRD demonstrates crystallite size, whereas SEM depicts the overall particle size, and one particle can have a set of crystallites.

UV-vis absorption and optical properties of synthesized material were characterized by UV-vis spectroscopy.
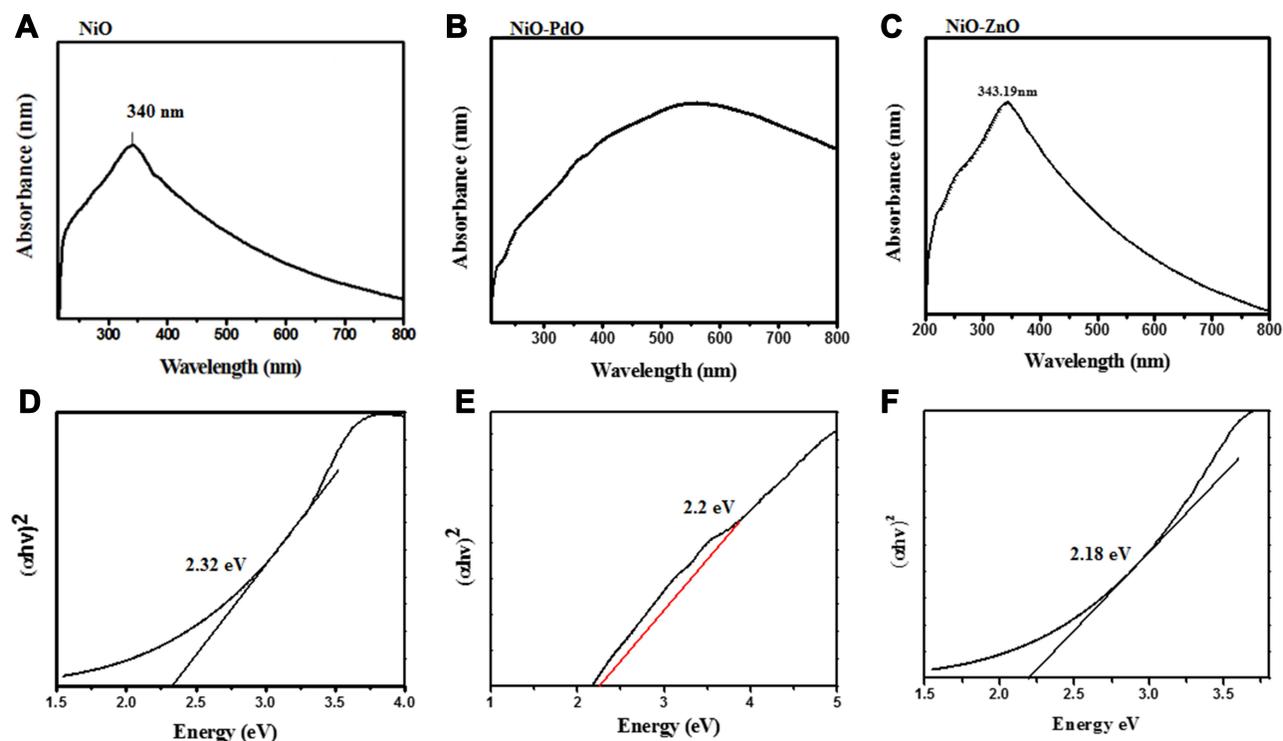
Figure 6 (**A–C**) Ultraviolet-visible absorption spectra of NiO, NiO–PdO, and NiO–ZnO; (**D–F**) Tauc plot of energy as $\alpha h v^2$ for NiO, NiO–PdO, and NiO–ZnO.

Figure 6A–C shows the absorption spectra of fabricated metal oxide NPs. Broad absorption range can be observed that gradually increases toward lower wavelengths, with maximum absorbance at 340 nm, a broad range of 300–700 nm, and 343.19 nm for NiO, NiO–PdO, and NiO–ZnO, respectively. The maximum absorption band indicates the presence of blue shift due to the presence of metal oxide. Figure 6D–F shows a Tauc plot determining the optical band-gap energy of synthesized material from UV absorbance. Using the following relationship, the band gap was derived:

$$\alpha h v = (h v - E g)\hat{}(n) \tag{3}$$

where α is the absorption coefficient, hv incident photon energy, and E_g optical band–gap energy. Nickel oxide is a wide band–gap semiconductor material with 3.2 eV band energy,[30] but in the present study the band gap calculated for NiO was 2.3 eV, mainly due to the incorporation of functional groups. When PdO and ZnO were incorporated into the NiO NPs, the band gap was reduced to 2.2 eV and 2.18 eV, respectively. The reduced band gap enhances the charge transfer properties of atoms between the conduction band and valence band. As such, the band gap was changed by incorporation of another metal oxide, producing a

synergic effect in the catalytic charge–carrier properties of the electrocatalyst. The lowest band gap was observed for NiO–ZnO, in good agreement with XRD and SEM results, in which NiO–ZnO particles were slightly larger and more separated than the other two oxides. It is well known that as particle size increases, the bandgap energy decreases,[32] and this was clearly observed in the present study also.

Catalytic Effects of Synthesized Nanomaterial on Dye Degradation

In order to investigate the catalytic activity of phytosynthesized NiO, NiO–PdO, and NiO–ZnO, reduction with MO was carried out by adding 2 mg catalyst in 10 mL MO stock solution (1 mg/mL) in light and dark ambient conditions. UV absorbance was monitored at different time intervals, i.e, 2 minutes, 5 minutes, 10 minutes, and 15 minutes and compared to the lambda maxima of MO (464 nm). The peak at 464 nm was that of an azo-bond due to n–π*. Another peak below 300 was also seen, which can be attributed to absorption of aromatic intermediates.[33] As shown in Figure 7A, the peak at 464 nm decreased with time, which demonstrates that azo-bond cleavage occured with synthesized catalysts. After 2 minutes, slight change in absorbance was observed in comparison with the blank without catalyst (S-1). With increasing time,
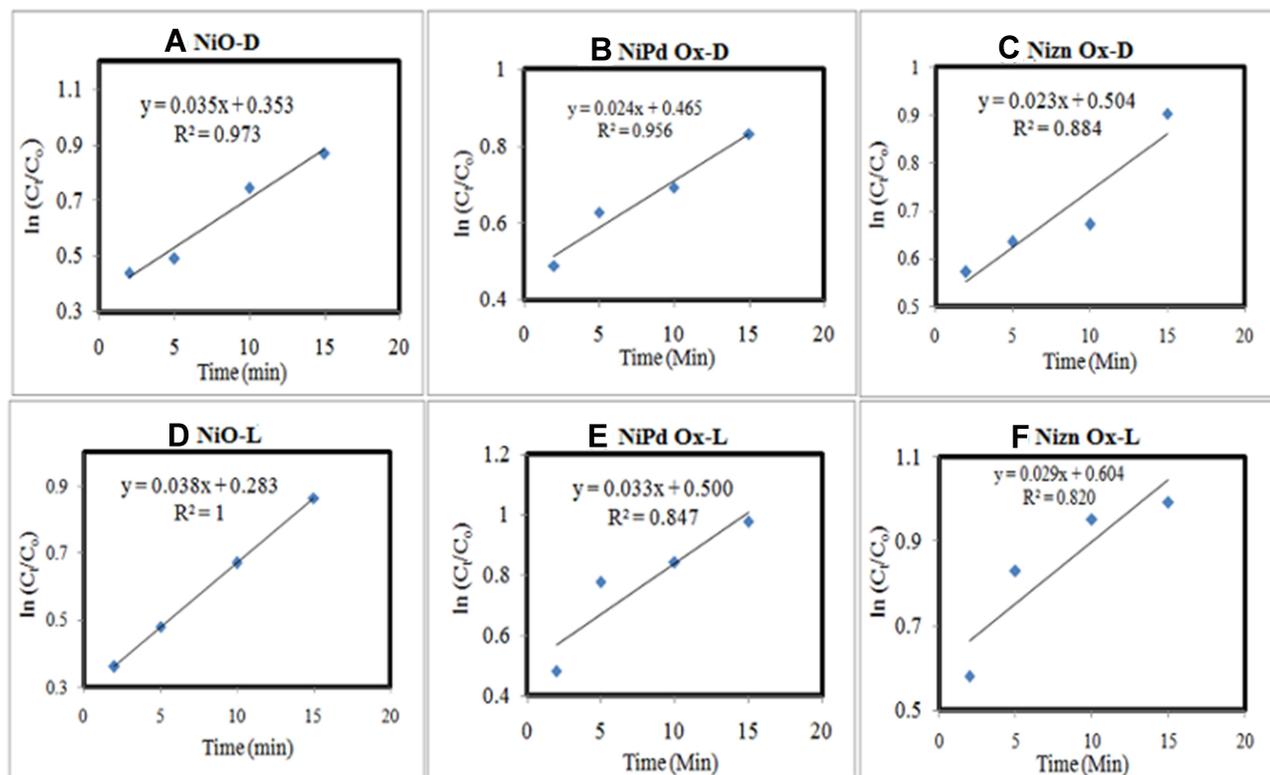
Figure 7 Ln (Ct–Co) vs time plot of (**A**) NiO-D, (**B**) NiO–PdO-D, (**C**) NiO–ZnO-D, (**D**) NiO-L, (**E**) NiO–PdO-L, and (**F**) NiO–ZnO-L.

absorbance intensity decreased to 0.4 nm. When the same sample (NiO) was observed in light, degradation occurred more quickly then in the dark. For NiO–PdO, a prominent decrease in absorbance maxima of MO was observed with increasing time in comparison with the blank sample, whereas the same sample in light showed a steadier decrease, due to the illumination source, which sped up catalytic performance. It can be seen in Figure 7E that after 15 minutes, absorbance was

closer to zero, which depicts maximum degradation of MO, and it was also observed visually that the solution became transparent over time. Figure 7C and F depicts the UV-vis absorbance of NiO–ZnO–loaded MO in dark and light, respectively. Even under dark conditions, the catalyst showed excellent catalytic performance, with decreased absorbance to 0.4 nm with 90% degradation within 15 minutes. This synergic activity of the catalyst could be a step toward a more
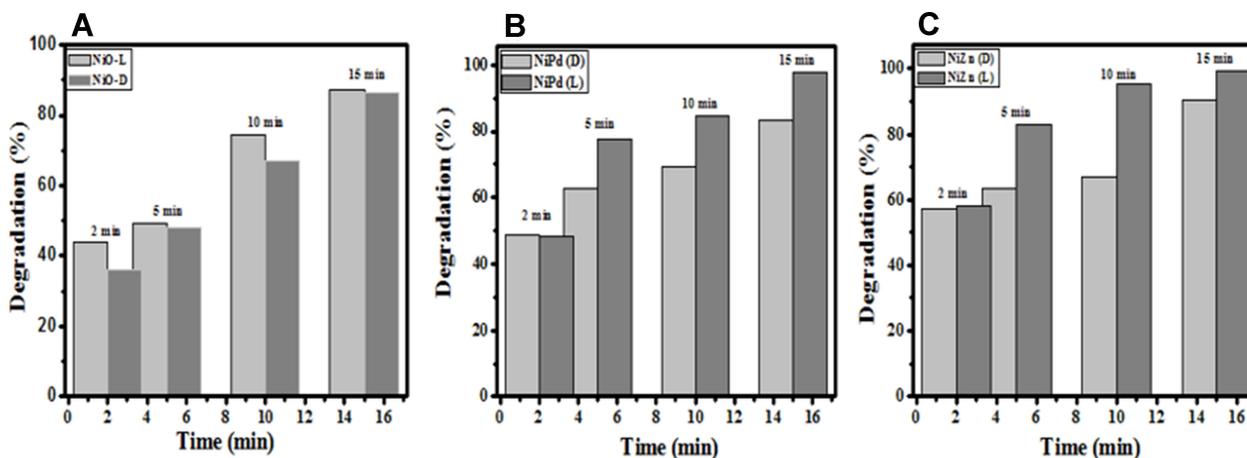
Figure 8 Percentage degradation of (**A**) NiO, (**B**) NiO–PdO, and (**C**) NiO–ZnO in light and dark conditions at different time intervals.

Table 1 Degradation percentage of MO by different catalysts in comparison with the blank

Time	NiO		NiO–PdO		NiO–ZnO		Blank	
	Light%	Dark%	Light%	Dark%	Light%	Dark%	Light%	Dark%
2 minutes	35.98	44	48.19	48.85	58.18	57.14	0	0
5 min	47.88	49.14	77.79	62.85	82.97	63.42	14.81	5.40
10 min	66.99	74.57	84.45	69.14	95.18	67.14	13.33	5.40
15 min	86.30	87.14	97.77	83.14	99.25	90.28	25.55	12.16

sustainable environmental remediation alternative, even in dark/ambient conditions.[34,35] The sample showed excellent catalytic performance in light, as shown in Figure 7F, in which almost 80% of MO degraded in the initial 5 minutes, and after 15 minutes the dye had completely degraded by breaking all the azo-bonds.[36] The enhanced degradation of MO by NiO–ZnO was attributed to the enhanced adsorption capacity of the nanocomposite. Incorporation of ZnO also improved surface area, which ultimately improved adsorption sites and degradation efficiency.

Reaction kinetics of catalytic degradation of MO via MOx catalyst was also evaluated from the calibration curve as shown in Figure 8. Calibration curves were constructed for lnC_t–C_0 vs time. In all samples, pseudo–first order kinetics were observed, as $R^2 < 1$).[37,38] R^2 values calculated for NiO, NiO–PdO, and NiO–ZnO in dark were 0.97, 0.5, and 0.884, respectively, whereas under solar radiation R^2 values for the three catalysts were 1, 0.87, and 0.842, depicting the stability and first-order reaction kinetics of the catalysts.

Degradation was also calculated from initial and final concentrations (eq. 1) of MO, as delineated in Table 1. All catalysts had potential for degradation of MO, with different percentage efficiency. NiO show good performance, even in dark conditions, with degradation % of 87% after 15 minutes. Compared to the single-metal oxide, the hybrid materials show good performance, eg, NiO–PdO, showed better activity under light, with 80% degradation in the first 10 minutes, while after 15 minutes the catalyst had achieved 97% removal. ZnO-incorporated NiO outperformed the other two catalysts, showing 90% efficiency in dark, while in light reaching ~100% efficiency within 15 minutes. As such, although all the catalysts had catalytic potential, NiO–ZnO gave the best results in terms of degradation efficiency. This can be attributed to the intermolecular junction created by p- and n-type materials. ZnO is naturally an n-type semiconductor, while NiO is a p-type semiconductor material. When ZnO was incorporated into p-type NiO, they

both made a p–n junction that made a synergic contribution to the movement of ions or charge-carrier molecules, enhancing the charge-transfer properties, and consequently improving the degradation of the single oxide.[39–41]

Conclusion

In the current study, three metal oxide nanostructures — NiO, NiO–PdO, and NiO–ZnO — were fabricated using an environmentally benign synthesis approach. XRD and EDX results confirm the pure formation of functionalized nanostructures. GC-MS and FTIR analysis revealed the involvement of phytoincorporated carbonaceous components in synthesized products. FESEM further showed the morphology of synthesized materials, which was ideal, with reduced agglomeration due to functionalization by organic compounds. The synthesized materials were successfully used for degradation of MO from water bodies under light and dark/ambient conditions. All three catalysts performed well in light, following first-order kinetics, but NiO–ZnO was particularly efficient, outperforming the others even in dark conditions, with probability of 90% in the first 15 minutes using only a small quantity of catalyst. The enhanced catalytic activity of NiO–ZnO could be attributed to increase numbers of protons by creation of p–n junctions that eventually increased the number of sites for catalytic reactions. Moreover, with biomimetic synthesis, the phytofunctionalized compounds facilitated protons due to organic compounds and also increased surface areas. Therefore, due to its efficient catalytic properties, phyto-fabricated NiO–ZnO is highly suitable for wastewater treatment and is a step toward a sustainable environment.

References

1. Gonawala KH, Mehta MJ. Removal of color from different dye wastewater by using ferric oxide as an adsorbent. *Int J Eng Res Appl*. 2014;4(5):102–109.
2. Dutta AK, Maji SK, Adhikary B. γ-Fe₂O₃ nanoparticles: an easily recoverable effective photo-catalyst for the degradation of rose bengal and methylene blue dyes in the waste-water treatment plant. *Mater Res Bull*. 2014;49:28–34. doi:10.1016/j.materresbull.2013.08.024
3. Predeseu A, Nicolae A. Univ."Politeh". *Bucharest Sci Bull Ser B*. 2012;74:1454–2331.
4. Faisal M, Tariq MA, Muneer M. Photocatalysed degradation of two selected dyes in UV-irradiated aqueous suspensions of titania. *Dyes Pigments*. 2007;72(2):233–239. doi:10.1016/j.dyepig.2005.08.020
5. Kumar A, Bisht BS, Joshi VD, Dhewa T. Review on bioremediation of polluted environment: a management tool. *Int J Environ Sci*. 2011;1(6):1079–1093.
6. Albanese A, Tang PS, Chan WC. The effect of nanoparticle size, shape, and surface chemistry on biological systems. *Annu Rev Biomed Eng*. 2012;14:1–16. doi:10.1146/annurev-bioeng-071811-150124
7. Sau TK, Rogach AL, Jäckel F, Klar TA, Feldmann J. Properties and applications of colloidal nonspherical noble metal nanoparticles. *Adv Mater*. 2010;22(16):1805–1825. doi:10.1002/adma.200902557
8. Tiwari JN, Tiwari RN, Singh G, Kim KS. Recent progress in the development of anode and cathode catalysts for direct methanol fuel cells. *Nano Energy*. 2013;2(5):553–578. doi:10.1016/j.nanoen.2013.06.009
9. Yu W, Xie H. A review on nanofluids: preparation, stability mechanisms, and applications. *J Nanomater*. 2012;2012:1–17. doi:10.1155/2012/435873
10. Alberi K, Nardelli MB, Zakutayev A, et al. The 2019 materials by design roadmap. *J Phys D: Appl Phys*. 2018;52(1):013001. doi:10.1088/1361-6463/aad926
11. Hasan M, Ullah I, Zulfiqar H, et al. Biological entities as chemical reactors for synthesis of nanomaterials: progress, challenges and future perspective. *Mater Today Chem*. 2018;8:13–28. doi:10.1016/j.mtchem.2018.02.003
12. Shamaila S, Sajjad AKL, Farooqi SA, Jabeen N, Majeed S, Farooq I. Advancements in nanoparticle fabrication by hazard free eco-friendly green routes. *Appl Mater Today*. 2016;5:150–199. doi:10.1016/j.apmt.2016.09.009
13. Gan PP, Li SFY. Potential of plant as a biological factory to synthesize gold and silver nanoparticles and their applications. *Rev Environ Sci Bio/Technol*. 2012;11(2):169–206. doi:10.1007/s11157-012-9278-7
14. Elumalai NK, Vijila C, Jose R, Uddin A, Ramakrishna S. Metal oxide semiconducting interfacial layers for photovoltaic and photocatalytic applications. *Mater Renew Sustain Energy*. 2015;4(3):11. doi:10.1007/s40243-015-0054-9
15. Upadhyay RK, Soin N, Roy SS. Role of graphene/metal oxide composites as photocatalysts, adsorbents and disinfectants in water treatment: a review. *RSC Adv*. 2014;4(8):3823–3851.
16. Shaheen I, Ahmad KS, Zequine C, Gupta RK, Thomas A, Malik MA. Organic template-assisted green synthesis of CoMoO₄ nanomaterials for the investigation of energy storage properties. *RSC Adv*. 2020;10 (14):8115–8129. doi:10.1039/C9RA09477F
17. Avcu E, Baştan FE, Abdullah HZ, Rehman MAU, Avcu YY, Boccaccini AR. Electrophoretic deposition of chitosan-based composite coatings for biomedical applications: a review. *Prog Mater Sci*. 2019;103:69–108. doi:10.1016/j.pmatsci.2019.01.001

18. Padil VVT, Černík M. Green synthesis of copper oxide nanoparticles using gum karaya as a biotemplate and their antibacterial application. *Int J Nanomedicine*. 2013;8:889.
19. Zahra T, Ahmad KS. Structural, optical and electrochemical studies of organo-templated wet synthesis of cubic shaped nickel oxide nanoparticles. *Optik*. 2020;205:164241. doi:10.1016/j.ijleo.2020.164241
20. Zahra T, Ahmad KS, Zequine C, Gupta RK, Thomas AG, Malik MA. Evaluation of electrochemical properties for water splitting by NiO nano-cubes synthesized using Olea ferruginea Royle. *Sustain Energy Technol Assess*. 2020;40:100753. doi:10.1016/j.seta.2020.100753
21. Ghotekar S. A review on plant extract mediated biogenic synthesis of CdO nanoparticles and their recent applications. *Asian J Green Chem*. 2019;3(2):187–200.
22. Jaffri SB, Ahmad KS. Augmented photocatalytic, antibacterial and antifungal activity of prunosynthetic silver nanoparticles. *Artif Cells Nanomed Biotechnol*. 2018;46(sup1):127–137. doi:10.1080/21691401.2017.1414826
23. Doll TE, Frimmel FH. Removal of selected persistent organic pollutants by heterogeneous photocatalysis in water. *Catalysis Today*. 2005;101(3–4):195–202. doi:10.1016/j.cattod.2005.03.005
24. Chen N, Shang H, Tao S, et al. Visible light driven organic pollutants degradation with hydrothermally carbonized sewage sludge and oxalate via molecular oxygen activation. *Environ Sci Technol*. 2018;52 (21):12656–12666. doi:10.1021/acs.est.8b03882
25. Liu H, Sha W, Cooper AT, Fan M. Preparation and characterization of a novel silica aerogel as adsorbent for toxic organic compounds. *Colloids Surf A Physicochem Eng Asp*. 2009;347(1–3):38–44. doi:10.1016/j.colsurfa.2008.11.033
26. Joshi P, Saxena P, Varshney MD, Rai VN, Mishra A. Effect of annealing temperature of CoCr2O4 on structural and vibrational properties. *Adv Sci Eng Med*. 2019;11(11):1079–1081. doi:10.1166/asem.2019.2456
27. Zhang Y, Ouyang J, Yang H. Metal oxide nanoparticles deposited onto carbon-coated halloysite nanotubes. *Appl Clay Sci*. 2014;95:252–259. doi:10.1016/j.clay.2014.04.019
28. Maruthupandy M, Zuo Y, Chen JS, et al. Synthesis of metal oxide nanoparticles (CuO and ZnO NPs) via biological template and their optical sensor applications. *Appl Surf Sci*. 2017;397:167–174. doi:10.1016/j.apsusc.2016.11.118
29. Thema FT, Manikandan E, Gurib-Fakim A, Maaza M. Single phase Bunsenite NiO nanoparticles green synthesis by Agathosma betulina natural extract. *J Alloys Compd*. 2016;657:655–661. doi:10.1016/j.jallcom.2015.09.227
30. Znad H, Abbas K, Hena S, Awual MR. Synthesis a novel multilamellar mesoporous TiO2/ZSM-5 for photo-catalytic degradation of methyl orange dye in aqueous media. *J Environ Chem Eng*. 2018;6 (1):218–227. doi:10.1016/j.jece.2017.11.077
31. Abbas KK (2018). Development of a Hybrid Multi-Functional Adsorbent-Solar-Photocatalyst for Detecting and Removing Toxic Heavy Metals and Refractory Pollutants from Water/Wastewater (Doctoral dissertation, Curtin University).
32. Ahmed AS, Singla ML, Naqvi AH, Naqvi AH, Azam A, Azam A. Band gap narrowing and fluorescence properties of nickel doped SnO2 nanoparticles. *J Lumin*. 2011;131(1):1–6. doi:10.1016/j.jlumin.2010.07.017
33. Zhong W, Jiang T, Dang Y, et al. Mechanism studies on methyl orange dye degradation by perovskite-type LaNiO3-δ under dark ambient conditions. Applied Catalysis A. *Appl Catal A*. 2018;549:302–309. doi:10.1016/j.apcata.2017.10.013
34. Soltani T, Entezari MH. Solar-Fenton catalytic degradation of phenolic compounds by impure bismuth ferrite nanoparticles synthesized via ultrasound. *Chem Eng J*. 2014;251:207–216. doi:10.1016/j.cej.2014.04.021
35. Chen J, Zhu L. Catalytic degradation of Orange II by UV-Fenton with hydroxyl-Fe-pillared bentonite in water. *Chemosphere*. 2006;65 (7):1249–1255. doi:10.1016/j.chemosphere.2006.04.016

36. Hua L, Ma H, Zhang L. Degradation process analysis of the azo dyes by catalytic wet air oxidation with catalyst CuO/γ-Al2O3. *Chemosphere*. 2013;90(2):143–149. doi:10.1016/j.chemosphere.2012.06.018

37. Moussavi G, Khosravi R. Removal of cyanide from wastewater by adsorption onto pistachio hull wastes: parametric experiments, kinetics and equilibrium analysis. *J Hazard Mater*. 2010;183(1–3):724–730. doi:10.1016/j.jhazmat.2010.07.086

38. Chen ZX, Jin XY, Chen Z, Megharaj M, Naidu R. Removal of methyl orange from aqueous solution using bentonite-supported nanoscale zero-valent iron. *J Colloid Interface Sci*. 2011;363(2):601–607. doi:10.1016/j.jcis.2011.07.057

39. Bai S, Li X, Kong Q, et al. Toward enhanced photocatalytic oxygen evolution: synergetic utilization of plasmonic effect and schottky junction via interfacing facet selection. *Adv Mater*. 2015;27 (22):3444–3452. doi:10.1002/adma.201501200

40. Berger C, Song Z, Li T, et al. Ultrathin epitaxial graphite: 2D electron gas properties and a route toward graphene-based nanoelectronics. *J Phys Chem B*. 2004;108(52):19912–19916. doi:10.1021/jp040650f

41. Dörling B, Ryan JD, Craddock JD, et al. Photoinduced p-to n-type switching in thermoelectric polymer-carbon nanotube composites. *Adv Mater*. 2016;28(14):2782–2789. doi:10.1002/adma.201505521

42. Lubbe A, Verpoorte R. Cultivation of medicinal and aromatic plants for specialty industrial materials. *Ind Crops Prod*. 2011;34(1):785–801. doi:10.1016/j.indcrop.2011.01.019